Materials Research. 2024; 27:e20240050
DOI: https://doi.org/10.1590/1980-5373-MR-2024-0050

Induced Martensitic Transformation Effect on Residual Stress, Fatigue and Magnetic Permeability of Austenitic Stainless Steel

Tiago Giordani**[a]**, Carla Adriana Theis Soares Diehl**[a*]**, Igor Luis Diehl**[a]**,

***Thomas Gabriel Rosauro Clarke**[a]*

[a]*Universidade Federal do Rio Grande do Sul, Laboratório de Metalurgia Física, Porto Alegre, RS, Brasil.*

Received: February 01, 2024; Revised: May 16, 2024; Accepted: June 04, 2024

This study aims at showing the influence of transformation-induced plasticity (TRIP) on the residual stresses and magnetic permeability of AISI 304 stainless steels and the resulting effect on its fatigue performance. Samples were pre-strained to different levels of plastic deformation, and characterised through metallography, hardness, tensile testing, X-ray diffraction (XRD) and with the MWM®-array electromagnetic method. Fatigue tests were then conducted on these samples to obtain the S-N curves for each condition, and the resulting fracture surfaces were analysed using scanning electron microscopy (SEM). Residual stress distributions in martensite and austenite were significantly affected by the transformation, although in different ways, and this is thought to be the reason for the improvement in fatigue performance in samples with higher pre-deformation values. Magnetic permeability measurements corroborated XRD results and proved to be a useful tool for non-destructively determining martensite transformation distributions in manufactured components.

Keywords: *Austenitic steel, residual stresses, fatigue, magnetic permeability.*

1. Introduction

Austenitic steels such as AISI 304 are widely used in the industry for their mechanical properties and corrosion resistance[1-3]. Due to their relatively low alloying element concentrations, these steels are metastable, and martensite formation may occur in processes involving sudden cooling or plastic deformation. The stability of austenite determines the rate of formation and the amount of martensite formed during mechanical forming processes, such as drawing, and it depends mainly on the steel composition, grain size, and morphology[4,5]. This transformation of austenite into α'-martensite during deformation, also known as Transformation-Induced Plasticity, or TRIP effect[6], leads to a significant increase in mechanical strength of the material[7]. Martensitic transformation also leads to an increase in residual stresses due to localized volumetric expansions resulting from the phenomenon[8].

When in operation, structures or components formed from metastable stainless steels can undergo repetitive and cyclic stresses, leading to fatigue damage[9]. There is no consensus on whether the effects of martensitic transformation are beneficial or detrimental in terms of fatigue resistance for these steels[10,11].

This study aims at assessing the TRIP effect on the fatigue performance of AISI 304 austenitic steel, as well as its influence on the variation of residual stresses and magnetic permeability. For this purpose, Wohler curves were generated for samples with different percentages of strain-induced martensite. Additionally, fatigue failure mechanisms were assessed through scanning electron microscopy (SEM). Phase and residual stress distributions in the near-surface region were analyzed by X-ray diffraction (XRD) to evaluate their respective influences on fatigue life. A Meandering Winding Magnetometer array (MWM®-array) was used to analyze the changes in magnetic properties after martensitic transformation, along the samples and at different depths; it is shown to be a promising as a non-destructive method that allows a rapid scan of the magnetic permeability of formed parts, indicating regions with different levels of martensitic transformation.

2. Material and Methods

2.1. Material and pre-strain tests

The material used was AISI 304 austenitic steel, in the form of a rolled sheet with a thickness of 4.5 mm. The chemical composition of the sheet used for specimen fabrication is described in Table 1.

The sheets were cut into standard test specimen shapes for tensile testing, as shown in Figure 1, using wire electrical discharge machining (WEDM) cutting, resulting in a rectangular cross-section specimen. The surfaces of the specimens were not modified after receiving the raw material. Tensile tests were conducted on an INSTRON Electromechanical Testing Machine with a maximum capacity of 210 kN. Displacement control was performed using a clip-gauge, while force control was carried out using the equipment's load cell. The gauge length considered was 25 mm. A loading rate of 0.5 mm/min was employed for tensile testing, following ASTM E8/E8M-21[12] standard. The

---

*e-mail: carla.adriana@ufrgs.br

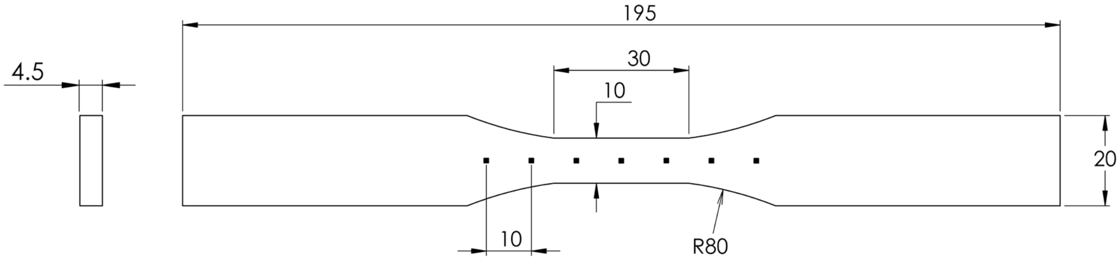

Figure 1. Schematic showing geometry and dimensions of the tensile test specimens, and points in which hardness and residual stress measurements were made. Units in mm.

Table 1. Chemical composition of the material.

	C	Si	Mn	Cr	Ni	Mo	N	Fe
Sample	0.06	0.42	1.08	17.46	8.66	0.17	0.0397	Bal.

following pre-strain deformation percentages were selected based on the stress-strain curve obtained from tensile tests: 5%, 10%, 15%, 20%, 25% and 30%. Vickers hardness testing was performed with an applied load of 125 kgf on seven points spaced at intervals of 10 mm along the center-line of the samples in the longitudinal direction as indicated in Figure 1. The residual stresses measurement as well as retained austenite determination were also performed at the same seven points indicated in Figure 1.

2.2. XRD

XRD measurements were taken at the same locations selected for hardness testing, but on the opposite surface of the samples. They were conducted using the Seifert Charon XRD M – Research Edition equipment from GE Inspection Technologies GmbH (Figure 2). The volume percent of austenite/martensite was determined by comparing the integrated XRD peaks intensity of ferrite and austenite phases with theoretical intensities through the Rayflex Analyze Version 2.503 software with the Austenite module. Measurements were carried out using Cr K_α radiation at an electric tension of 30 kV and a current of 30 mA, with suppression of the respective K_β lines through a vanadium film.

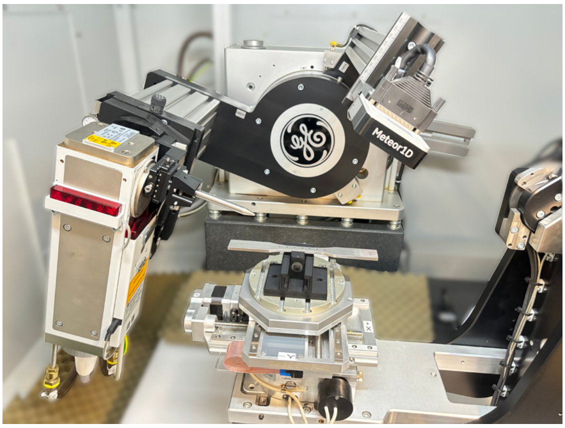

Figure 2. X-ray diffractometer model Seifert Charon XRD M – Research Edition.

2.2.1. Phase Analysis

The relative intensities of the martensite diffraction peaks $\alpha'(110)$, $\alpha'(200)$, and $\alpha'(211)$ were compared with the diffraction peaks of retained austenite $\gamma(111)$, $\gamma(200)$, and $\gamma(220)$. The use of this number of peaks avoids potential biases due to crystallographic texture[13]. Phase analysis was performed using a 2θ range between 50° and 166° with a step of 0.01°. Curve fitting of the diffraction peaks was carried out following the Pseudo Voigt model with background correction, and the volume percentage of retained austenite was determined by comparing the integrated intensities of martensite and retained austenite in accordance with ASTM E975-13[14].

The volumetric fraction of each phase was determined through a procedure based on the method presented by Faninger and Hartmann[15]. In this procedure, the austenite fraction, X^γ, was calculated from the average of the ratios of the integrated intensities of each martensite diffraction peak $I_{\alpha'}$ – $\alpha'(110)$, $\alpha'(200)$ and $\alpha'(211)$ – and austenite, I_γ – $\gamma(100)$, $\gamma(200)$ and $\gamma(220)$ – in combination with correction factors R as in Equation 1. The R factors are presented in Table 2.

$$X^{\gamma} = \left(\frac{I_{\alpha'}}{I_{\gamma}} . \frac{R_{\gamma}}{R_{\alpha'}} + 1 \right)^{-1} \tag{1}$$

2.2.2. Residual stresses analysis

The residual stresses were determined using the $\sin^2\psi$ method, in iso-inclination mode, on the surface of the samples and at depths of 50 μm and 100 μm. For austenite, the $\gamma(220)$ peak was measured with 2θ ranging from 119° to 137° at a scan step of 0.1°. For martensite, the $\alpha'(211)$ peak was obtained with 2θ ranging from 146° to 165° using a scan step of 0.2°. The elastic constants for the γ-Fe and α-Fe phases were $½s_2 = 6.19\text{x}10^{-6}$ MPa^{-1}, $s_1 = -1.36\text{x}10^{-6}$ MPa^{-1}, and $½s_2 = 5.81\text{x}10^{-6}$ MPa^{-1}, $s_1 = 1.27\text{x}10^{-6}$ MPa^{-1}, respectively. These elastic constants were used for stress calculations using the Analyze software. To remove layers for depth analyses, an electrolytic solution composed of 42% phosphoric acid (H_3PO_4), 34% sulfuric acid (H_2SO_4), and 24% distilled water was employed. A micrometer was used to control the depth. Measurements after layer removal were taken at the same positions as the hardness measurements.

Table 2. R factors for austenite and martensite with Cr-K$_\alpha$ radiation (Faninger and Hartmann[15]).

Austenite hkl	2θ (°)	R-Factor (10^{-48} cm^{-6})	Martensite hkl	2θ (°)	R-Factor (10^{-48} cm^{-6})
111	66.8	77.2	110	68.8	105.0
200	79.0	36.6	200	106.0	23.4
220	128.7	57.1	211	156.1	237.0

The procedure described above for residual stress measurements is referred to here as the standard analysis. The procedure described below is used for residual stress analysis in a state of triaxial stress. The evaluation of residual stress measurements using the standard $\sin^2\psi$ method is based on the assumption that a plane stress state with the normal component, σ_{33}, equal to zero is present due to the low penetration depth of the Cr-K$_\alpha$ radiation. In a material consisting of two or more phases, σ_{33}^k (the superscript k refers to martensite, α', or austenite, γ), as well as σ_{13}^k and σ_{23}^k, may exist in different phases as pseudo-macrostress (type II residual stresses). Thus, the evaluation of residual stresses by XRD in the case of multiphase samples requires that the value of the lattice parameter under stress-free conditions, d_0^k, be determined with great accuracy[16,17]. Data on d_0^k available in the literature may not always be used since it cannot be guaranteed that the material of the sample of interest has undergone exactly the same thermomechanical processes as the materials from the available publications[16]. Thermomechanical processes can systematically alter the lattice parameter through variations in chemical composition, dissolved elements, precipitates, dislocation density, and stacking faults[18].

According to Fitzpatrick and Lodini[16], there are several techniques that allow the experimental determination of d_0^k from the sample itself to be analyzed. One of these techniques involves the use of stress relief treatments; however, high temperature activates diffusional processes and may promote changes in the proportions of phases and dissolved elements in each of them.

A second possibility is powder analysis made with the sample itself, which is genuinely free of macroscopic stresses. However, powder production processes typically involve thermomechanical processes that are not the same as those of the sample of interest, making the use of powders for determining d_0^k inappropriate.

In this work, stress-free samples were obtained by producing coupons from the samples of interest, reducing their size until they are small enough to relieve a significant portion of the residual stresses and especially to ensure that the entire volume is illuminated by the X-ray beams. Since a body devoid of external loads and at rest is in equilibrium, the integral of residual stresses over the sample volume results in a zero resultant force. Therefore, by analyzing the 2θ position of the diffraction peaks and, using Bragg's Law, calculating the lattice parameter, an approximate value of d_0^k is obtained. The coupons were produced to determine $d_0^{\alpha'}$ and d_0^{γ} for the martensite and austenite phases, respectively, from samples with 0%, 15%, and 30% deformation, which were chemically etched to achieve samples with lateral dimensions of 1 mm x 1 mm and a thickness of 20 μm. The layer removal method identical to that used for measuring subsurface residual stresses was employed. Spinning and tilting χ up to 60° of the diffractometer were used to obtain the approximation of d_0^k through its average for various directions. The measurement uncertainty associated with the analysis of d_0^k, δd, was calculated from the Goodness of Fit of the curve fitting of the diffraction peaks and using uncertainty propagation from Equation 2.

$$\delta d = \left|\frac{\partial d}{\partial 2\theta}\right| \times \delta 2\theta \qquad (2)$$

where $\delta 2\theta$ is the measurement uncertainty of the 2θ position of the diffraction peak. The quantity of calibration samples was limited by the difficulty of obtaining them and covered the surface of the sheet used as raw material. These data were used for calculating residual stresses both on the surface and in the core of the samples, and linear interpolations were performed to estimate d_0^k for samples with pre-deformation of 5%, 10%, 20%, and 25%.

The penetration of the X-ray beams into the sample varies from 25.0 μm to 12.5 μm while χ varies from 0° to 60°. Therefore, the value of d_0^k obtained by the procedure described above is considered an approximation of the true value, and thus an iterative method, as indicated by Hauk[17:242], had to be performed to minimize the value of σ_{33}. After the refinement of d_0^k, σ_{33}^k for each phase was calculated using Equation 3[17], once macroscopic stress is calculated as a weighted average of the pseudo-macrostresses over each phase, with the proportion of each phase's content serving as the weight in the average calculation[19]. The values of σ_{11}^k and σ_{22}^k for each phase can be calculated using Equation 4, where ($\sigma_{11}^k - \sigma_{33}^k$) and ($\sigma_{22}^k - \sigma_{33}^k$) are the residual stress values obtained with the standard $\sin^2\psi$ method in the 11 and 22 directions, respectively. The macroscopic stresses σ_{11}^{macro} and σ_{22}^{macro} were calculated using Equation 5. The macroscopic residual stresses in the 33 direction, calculated using Equation 6, should be zero.

$$\sigma_{33}^k = \frac{1}{3s_1^k + \frac{1}{2}s_2} \times \left[\left(\frac{d_+^k - d_0^k}{d_0^k}\right) - 2s_1^k\left(\sigma_{11}^k - \sigma_{33}^k\right)\right] \qquad (3)$$

$$\sigma_{11}^k = \left(\sigma_{11}^k - \sigma_{33}^k\right) + \sigma_{33}^k ; \sigma_{22}^k = \left(\sigma_{22}^k - \sigma_{33}^k\right) + \sigma_{33}^k \qquad (4)$$

$$\sigma_{11}^{macro} = \sum \left(\sigma_{ii}^k \times X^k\right), \sigma_{22}^{macro} = \sum \left(\sigma_{22}^k \times X^k\right) \qquad (5)$$

$$\sigma_{33}^{macro} = \sum \left(\sigma_{33}^k \times X^k\right) = 0 \qquad (6)$$

σ_{ii} is the residual stress in a direction ii, s_1 and $\frac{1}{2}s_2$ are the elastic constants of the considered phase, k represents the austenite or martensite phases, X^k is the fraction of the considered phase, d_+ and d_0 are the interplanar spacings of the stressed and stress-free samples, respectively.

2.3. Fatigue testing

Fatigue tests were conducted on as-received material specimens (0% pre-deformation) and on specimens deformed by 5%, 15%, and 25%. At least three samples per condition were used. The axial tension-tension fatigue tests were conducted on an MTS Model 810 universal servo-hydraulic testing machine. The standard followed for the tests was ASTM E466-21[20]. A frequency of 35 Hz was used, the R ratio was 0.1, and the number of cycles considered as run-out was determined to be 1 million cycles.

For the analysis of fractures in the samples broken during the fatigue test, the samples were sectioned and examined with a scanning electron microscope (SEM). For this purpose, the surface containing the fracture was sectioned from the rest of the sample. This surface underwent initial cleaning with water, liquid detergent, and a soft brush. Subsequently, the fractured section underwent ultrasonic bath in acetone and subsequent drying.

2.4. MWM

The Meandering Winding Magnetometer (MWM) technique was used to measure the relative magnetic permeability of the specimens. The jET system (JENTEK® Eddy Current Tester) was employed; it was equipped with a 7-channel MWM-array sensor FA316 and an integrated encoder for displacement recording. Scans were performed on the surface and subsurface in the longitudinal direction of each specimen. The jET system is shown in Figure 3.

3. Results

3.1. Mechanical-metallurgical characterisation

Table 3 presents the mean values of mechanical properties and the standard deviations obtained through tensile testing at room temperature for three samples. This material does not exhibit a yield plateau, and the yield strength is determined using the offset method with the start of the line at a deformation of 0.2%.

The stress-strain curve of the material is shown in Figure 4. The levels of deformation applied to the specimens were defined based on the linear region of the stress-strain curve. The unstable flow (“serrations”) present in the region near the maximum stress of the tensile graph is caused by the formation of deformation-induced martensite. Dislocation slip in austenite and the formation of martensite by deformation are considered competitive modes of plastic deformation[21]. The drop is due to constriction, which creates a geometric instability and a stress concentrator, which in turn generates the triaxial state.

The measurement error for the clip gauge used in the tensile tests is 1% or 0.2 mm, whichever is greater. The measurement uncertainty of the load cell is at most 0.78% or 0.009 kN.

Furthermore, micrographs of the as-received samples and with 30% deformation were obtained, as shown in Figure 5a and b respectively. In the micrographs, the white region corresponds to austenite, and the dark region corresponds to martensite. It can be visually observed in the micrograph of the sample with 30% deformation shown in Figure 5b that the darker region increases compared to the as-received sample shown in Figure 5a.

Figure 6 shows the Vickers hardness profile measured at seven points on the surface of each sample. It is observed that there is an increase in hardness with the formation of strain-induced α'-martensite. The hardness value of the as-received material was 217 HV, while the difference between the as-received material and the sample with 30% deformation was 130 HV in the central region of the sample. Regarding the hardness measurements, the measurement uncertainty associated with the equipment used is 1.3% or 5.8 HV.

3.2. XRD Analysis

Figure 7 shows the XRD diffractogram of AISI 304 steel with different levels of deformation. After analysis, it was found that the surface of the as-received (AR) sheet

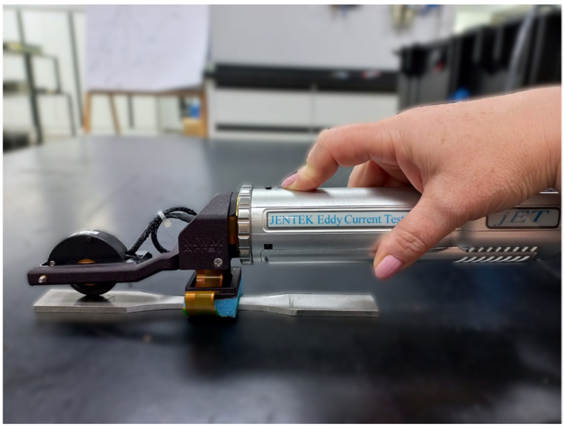

Figure 3. JENTEK Eddy Current hand-held jET Tester.

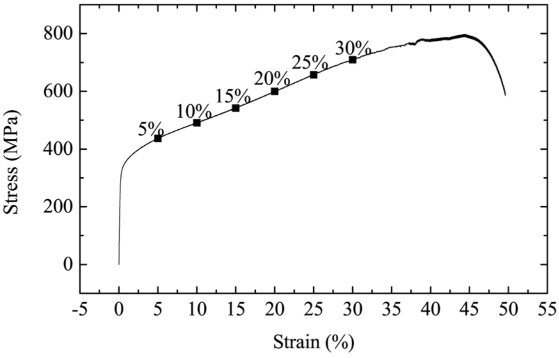

Figure 4. Example of stress - strain curve of a AISI 304 sample.

Table 3. Mean values of mechanical properties of the material.

Mechanical Properties	Yield Strength (MPa)	Ultimate Strength (MPa)	Stress at Fracture (MPa)	Elongation at Fracture (%)
AISI 304	326.9	810.8	612.3	53.2
Standard Deviation	14.54	15.58	41.43	0.03

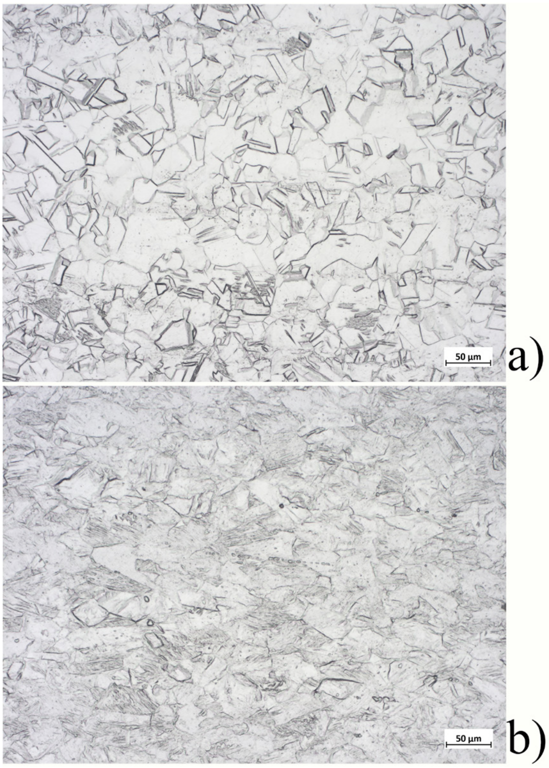

Figure 5. Micrographs of the (a) as received and (b) 30% deformation samples. Magnification 200x, electrolytic etching with oxalic acid, 8V, 12 minutes.

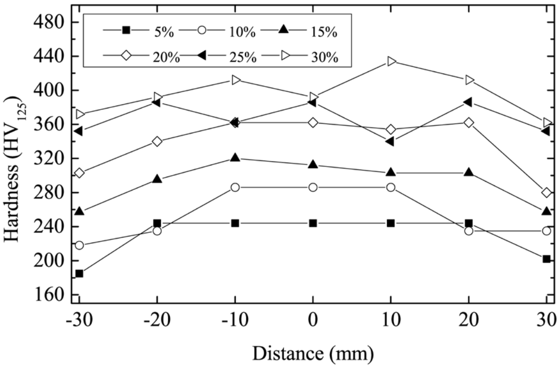

Figure 6. Vickers hardness results on the surface of each pre-strained sample, relative to the center of the sample.

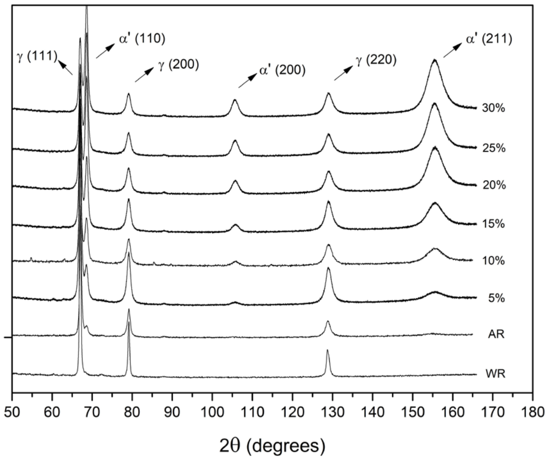

Figure 7. XRD diffractograms obtained for each pre-strained sample of AISI 304 (AR means as received and WR means with layer removal).

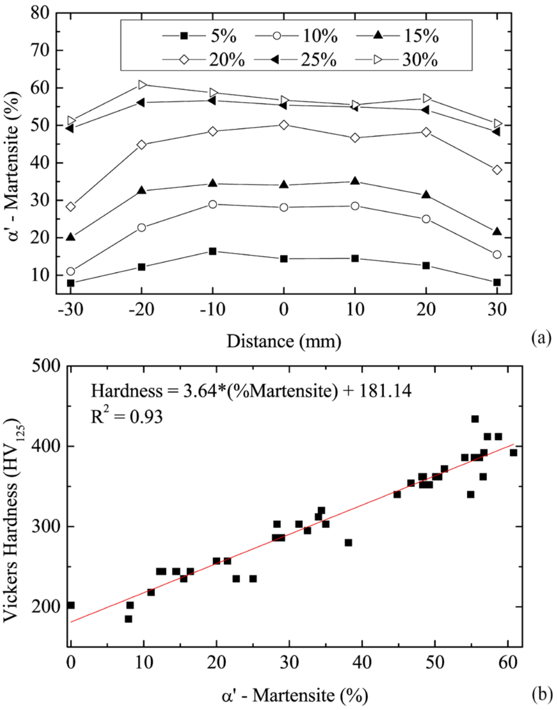

Figure 8. (a) *α'*-martensite volume content for samples with different pre-strain deformation values, measured by XRD; and (b) correlation between hardness and *α'*-martensite volume content.

contains more martensite than the material core (WR), where two peaks *α'*(110) and *α'*(211) were observed in the AR sample, indicating the presence of a pre-existing surface modification in the raw material, possibly caused by the final rolling stage. The profile of the as-received material exhibits prominent austenite peaks *γ*(111), *γ*(200), and *γ*(220). The non-ferromagnetic HCP *ε*-martensite phase is not easily detected by diffraction analysis. According to Zeng et al.[22], the *γ*→*ε* transformation occurs before the *γ*→*α'* transformation, and generally, the transformation sequence is *γ*→*ε*→*α'*[22-24]. In diffraction pattern analyses, a phase is identified through three peaks, and in the samples of this study, the presence of the *ε*-martensite peaks could not be observed. On the other hand, the formation of *α'*-martensite can be observed from the first level of deformation by the presence of peaks *α'*(110), *α'*(200), and *α'*(211).

The volume percentage of *α'*-martensite obtained by the Austenite module of the Analyze software is shown in Figure 8a. An increase in the percentage of *α'*-martensite is observed, reaching 88% in the sample with 30% deformation compared to the sample with 0% deformation, where the martensite percentage is 6%. The reduction in the percentage of *α'*-martensite at positions -30 mm and +30 mm is due to a lower level of deformation at these points, which, it is worth noting, are outside the analysis area considered in tensile test. Figure 8b demonstrates the expected increase in hardness values with the increase in the volume percentage of martensite[25]. According to ASTM E975[14] standard, the measurement uncertainty due to random errors related to retained austenite measurements was estimated at 4% with a confidence level of 95%. Regarding systematic errors related to the determination of retained austenite, there is no estimation of measurement uncertainties because there is no independent method to determine an acceptable reference value.

Figure 9a presents the values of d_0^k measured from samples with 0%, 15%, and 30% pre-deformation (filled markers). It is possible to observe that the measurement uncertainty of the lattice spacing varies with pre-deformation. This occurs because the proportion of martensite increases with plastic deformation, as can be seen in the diffraction patterns in Figure 7, and consequently, the signal of its diffraction peak intensifies, increasing the signal-to-noise ratio. In Figure 7, the peaks corresponding to the martensite phase in the sample without pre-deformation are not visually evident due to its low concentration of 6%. Conversely, with the austenite phase, the effect is opposite; the signal-to-noise ratio worsens with increasing pre-deformation, as its presence diminishes. The initial estimates for d_0^k from samples with 5%, 10%, 20%, and 25% pre-deformation, interpolated from the data of samples with 0%, 15%, and 30% pre-deformation, are shown in Figure 9a (unfilled markers). The data in Figure 9a were refined according to the procedure described in subsection 2.2.

The interplanar spacings in samples under stress (d_+^k) and stress-free (d_0^k) of the austenite phase γ(220) and the martensite phase α'(211) are shown in Figure 9b, where the two phases are compared. It is a common practice to use d_+^k as an approximation of d_0^k; however, the data in Figure 9b show differences of up to 0.0015 Å between $d_+^{\alpha'}$ and $d_0^{\alpha'}$ and 0.0012 Å between d_+^{γ} and d_0^{γ}, indicating that this practice may result in gross errors in the analysis of residual stresses in AISI 304 steel. A significant difference in the values of d_0^k and d_+^k in both phases can be observed from the sample without pre-deformation compared to the pre-deformed samples. This difference may be due to the thermomechanical processes that the samples underwent. Since the raw material is a sheet, the stress state in the as-received (AR) sample is presumably due to the rolling process. There is not enough information to infer the rolling temperature of the raw material, but, considering that there is presence of martensite phase only on the surface (Figure 7), one can conjecture assuming that the rolling was done at high temperature, but the surface lost heat between the heating stages and the final rolling pass. On the other hand, the pre-deformed samples experienced cold tensile deformation without any input of heat, which can significantly alter the microstructure compared to a sample deformed at high temperature.

The standard residual stress analysis in the longitudinal direction ($\sigma_{11}^k - \sigma_{33}^k$) and transverse direction ($\sigma_{11}^k - \sigma_{33}^k$), macroscopic residual stresses σ_{11}^{macro} and σ_{22}^{macro}, and pseudo-macrostress σ_{11}^k and σ_{22}^k are shown in Figure 10a and Figure 10b, respectively.

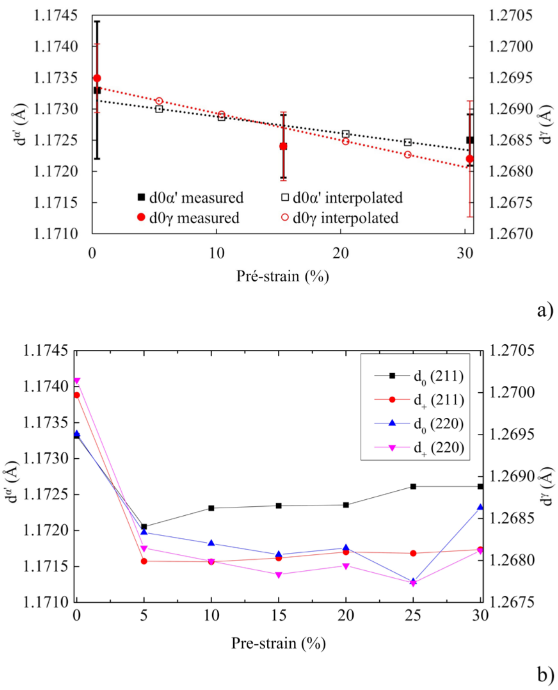

Figure 9. Interplanar spacing of austenite γ(220) and martensite α'(211) as a function of pre-strain deformation. a) measured data and interpolations and b) refined values of d_0^k and d_+^k.

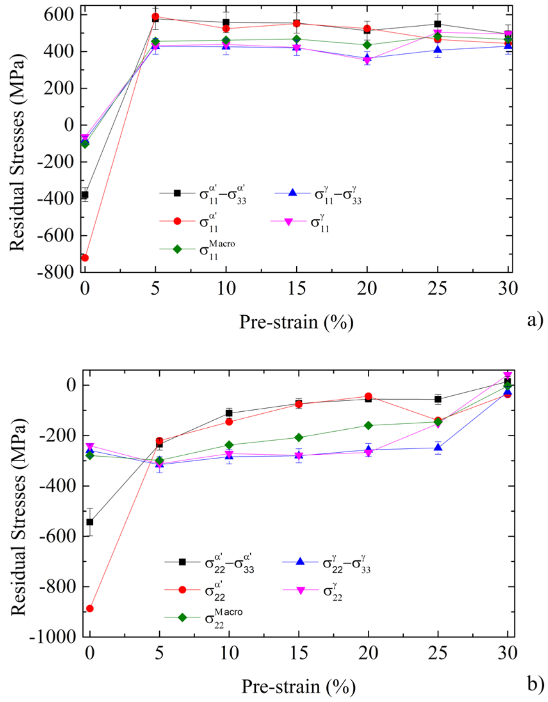

Figure 10. Surface residual stresses evolution in the (a) longitudinal and (b) transversal directions, as a function of pre-strain deformation.

The value of standard surface residual stresses ($\sigma_{11}^{\alpha'} - \sigma_{33}^{\alpha'}$), shown in Figure 10a for the as-received sample (0% pre-deformation) was -377 MPa, while upon applying loading, the values became tensile, reaching a maximum of 577 MPa if the *α'*(211) phase is analyzed. Upon analyzing the values of $\sigma_{11}^{\alpha'}$, changes in stress value can be observed from -720 MPa compressive in the unloaded sample to 590 MPa tensile in the sample deformed by 5%. The residual stresses in the *γ*(220) phase exhibited the same behavior as those obtained in the *α'*(211) phase, but to a lesser extent. The ($\sigma_{11}^{\gamma} - \sigma_{33}^{\gamma}$) stresses ranged from a minimum of -82 MPa in the 0% pre-load sample to a maximum of 428 MPa in the 30% pre-load sample. The σ_{11}^{γ} stresses ranged from -64 MPa to 504 MPa, similar to the values of σ_{11}^{macro}, which ranged from -103 MPa to 482 MPa. The values of residual stress in the longitudinal direction, from the 5% pre-deformation onwards, did not show significant changes with increasing applied load.

The initial state of residual stresses in the as-received sample can be attributed to the thermo-mechanical rolling process, which is known to result in residual stresses in AISI 304 sheets[26] and is generally employed in the manufacturing of metallic sheets. After tensile deformation, the tensile residual stresses can be attributed to the minor plastic deformations suffered by the surface compared to the core. Since the thermo-mechanical processes are not uniform in the manufacturing of the raw material sheet, the surface presumably has a higher yield strength than the core. An indication of this is the presence of martensite on the surface, which is absent in the core, as can be seen in the diffraction patterns in Figure 7. Having a higher yield strength, the surface will experience less plastic deformation than the core, and thus, the elastic recovery of the surface will be greater. However, the elastic recovery of the surface will be hindered by the core, generating tensile residual stresses, as those observed in Figure 10a. Another indication that supports this hypothesis can be found in Figure 11a, where the residual stresses at 0.05 mm and 0.1 mm are considerably lower than the residual stresses at the surface, considering the samples with pre-deformation.

On the other hand, the residual stresses in the transverse direction in Figure 10b exhibited a compressive state in all analyzed samples, tending to zero with increasing loading. The unloaded sample showed standard residual stresses ($\sigma_{22}^{k} - \sigma_{33}^{k}$) with compressive values of -543 MPa and -259 MPa in the *α'*(211) and *γ*(220) phases, respectively. The stresses $\sigma_{22}^{\alpha'}$ and σ_{22}^{γ} for the unloaded sample showed values of -887 MPa and -240 MPa, respectively. The stresses in the loaded samples, on the other hand, ranged from -310 MPa (5% pre-load) to 0 MPa (30% pre-load). It is expected that uniform plastic deformations relieve the residual stresses of a given component, especially in the direction transverse to the loading. The results of residual stresses in the transverse direction indicate that the plastic deformations, up to the 25% pre-deformation, imposed on the components were not sufficient to achieve complete relief of residual stresses.

The subsurface residual stresses σ_{11}^{k} shown in Figure 11a also do not change with increasing loads beyond 5%. However, there is a significant reduction of over 400 MPa in the value of subsurface stresses compared to surface stresses. On the other hand, the subsurface residual stresses σ_{22}^{k} showed surface values around -300 MPa, while at a depth of 0.1 mm, the stresses remained between -100 MPa and 0 MPa, as can be seen in Figure 11b. It was not possible to calculate $\sigma_{11}^{\alpha'}$ and $\sigma_{22}^{\alpha'}$ at a depth of 0.1 mm in the as-received and 5% pre-deformed samples because the martensite fraction in these samples is not sufficient for the identification of the respective diffraction peaks. The results found at depth of 0.1 mm can be compared with the predictions of Msolli et al.[19], taking into account the measurements uncertainties, which found low compressive residual stress in austenite and significant tensile residual stress in martensite.

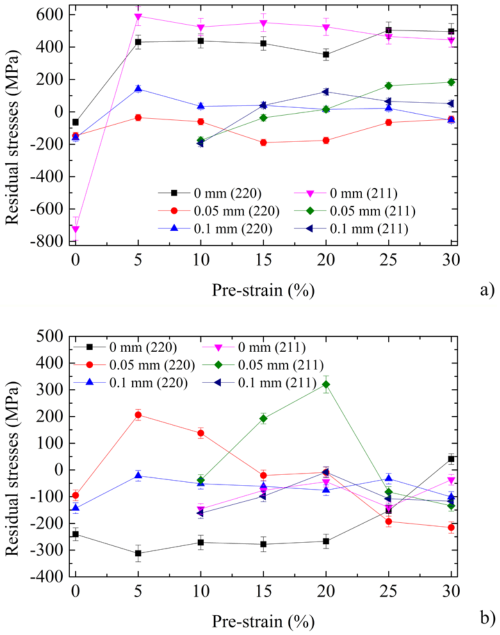

Figure 11. Residual stress evolution in martensite (211) and austenite (220) phases, as a function of pre-strain deformation, at different depths in the (a) 11 direction and (b) 22 direction.

In relation to residual stress measurements by X-ray diffraction, the measurement uncertainty due to random errors is 20 MPa. The measurement uncertainty due to the fitting of the 2θ curve by intensity, which is based on the signal-to-noise ratio, was defined as a maximum of 10% of the measured value. According to ASTM 2860[27] standard, there is no estimation of measurement uncertainties for systematic errors in residual stress measurements because there is no independent method to determine an acceptable reference value.

3.3. MWM

Figure 12a shows the variation of magnetic permeability relative to air, measured on the surface and at 50 µm depth, and 100 µm depth using the MWM-array system. Subsurface measurements were conducted after removing a layer from the samples. The equipment performs measurements using three different frequencies. It can be observed that there is no significant variation in magnetic permeability between the sample with 0% and 5% applied deformation. However, the relative magnetic permeability increases with applied deformation due to the evolution of ferromagnetic martensite during the induced transformation[28]. The permeability is reduced with the removal of the layer regardless of the analyzed frequency. The penetration depth achieved by the

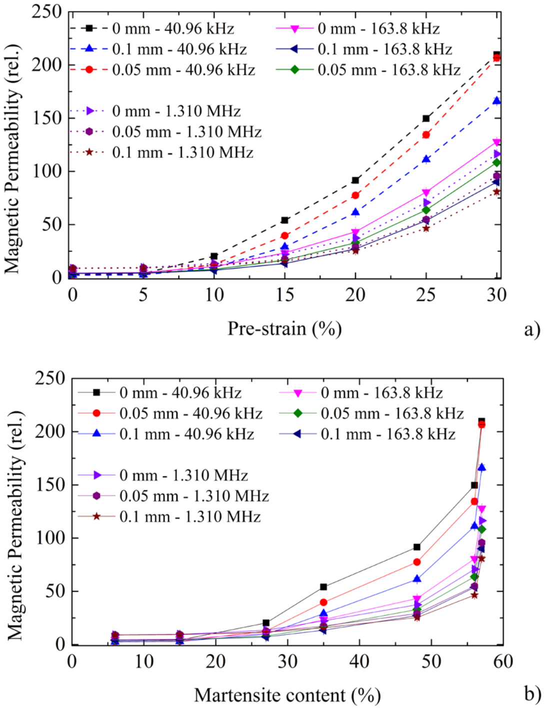

Figure 12. Permeability variation in different depth and frequencies as a function of (a) pre-strain deformation and (b) α'Martensite.

MWM-array sensor, according to Washabaugh et al.[29], varies with frequency, spatial wavelength of the winding λ, and the material being evaluated. For stainless steel with a spatial wavelength of 0.5 inches, the penetration depth is about 2 mm at $f = 1$ kHz and decreases to 0.5 mm at $f = 1$ MHz.

Figure 12b shows the correlation between magnetic permeability and martensite percentage. It can be observed that the magnetic permeability does not undergo significant changes for an α'-martensite percentage below 30%, equivalent to a pre-load of 10%. However, there is a considerable increase in permeability for percentages greater than 50% of α'-martensite.

According to Cao and Iwamoto[30], magnetic permeability is related to the amount of martensite. As observed in Figure 8a, the deformation-induced martensite content measured by XRD on the surface of the specimens increases with applied load. The same trend is observed in Figure 12, where magnetic permeability on the surface also increases with the increasing load in the samples, reaching its maximum value in the sample with 30% deformation.

Figure 13a, b, c, d, and e show the magnetic permeability C-scan along the surface of the samples with 30%, 25%, 20%, 15%, and 10% deformation, respectively. In Figure 13f, the profile of relative magnetic permeability is observed by the sensor position acquired by 3 channels on the surface of all samples. The frequency used in Figure 13 was 1.31 MHz. An increase in magnetic permeability with applied load on the samples is noticeable, and no significant variations between the channels of the sensor can be observed. The unloaded sample showed values close to zero of relative magnetic permeability, with no significant increase with the application of 5% pre-loading. However, after 10% deformation, a significant increase in relative magnetic permeability can be observed.

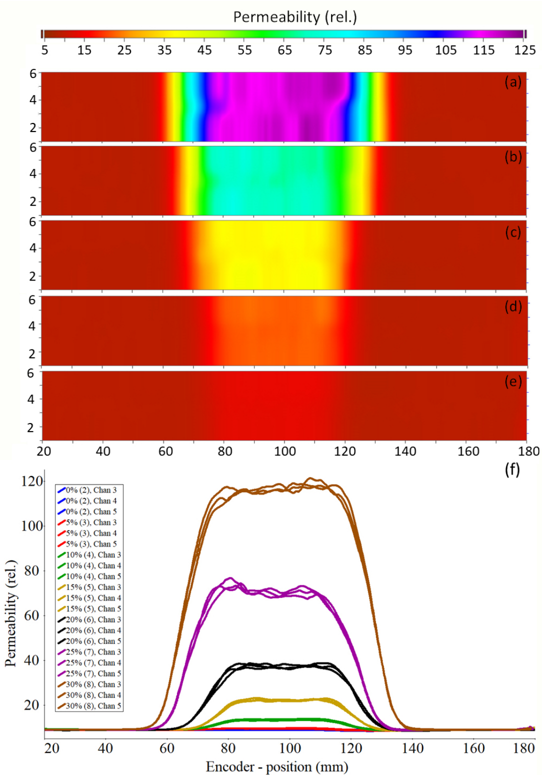

Figure 13. C-scan magnetic permeability of the sample with pre-strain deformation of (a) 30%, (b) 25%, (c) 20%, (d) 15% and (e) 10% deformation. Additionally, (f) the magnetic permeability along the central line, as measured by encoder position, from channels 3, 4, and 5 for each pre-strain deformation sample.

3.4. Fatigue testing

Figure 14 displays the S-N curve of samples with no deformation, 5%, 15%, and 25% deformation. It is possible to observe an increase in maximum stress with the increase in loading or the percentage of martensite, with the samples at 25% deformation exhibiting a longer fatigue life than those with lower deformations. Samples with 25% deformation showed an ultimate tensile strength of 478 MPa at 10^6 cycles, followed by samples with 15% (418 MPa), samples with 5% (398 MPa), and finally, samples with 0% showing the lowest ultimate tensile strength of 339 MPa. These results indicate that increasing the level of pre-strain in metastable AISI 304 austenitic steel samples enhances the ultimate tensile strength[25,31]. This is attributed to the increase in dislocation density caused by the applied deformation[31].

The specimens were subjected to axial tension-tension fatigue loading, with crack propagation and final fracture perpendicular to the loading axis, promoting crack initiation on the surface in most samples. This initiation typically occurs at the corner of the samples, as shown in Figure 15a, due to the highest stress concentration at that point. The surface fatigue crack initiation is facilitated by the tensile stresses that occur on the surface of samples with induced deformation[9,32].

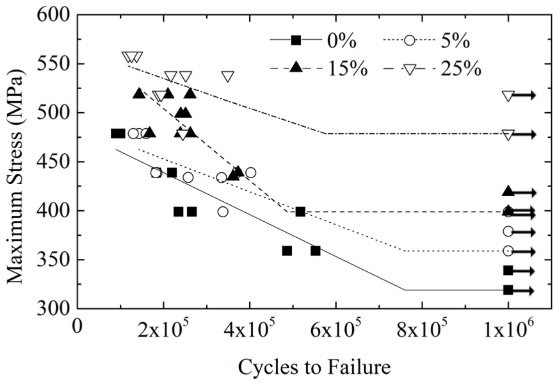

Figure 14. S-N curves obtained from different pre-strain deformation levels.

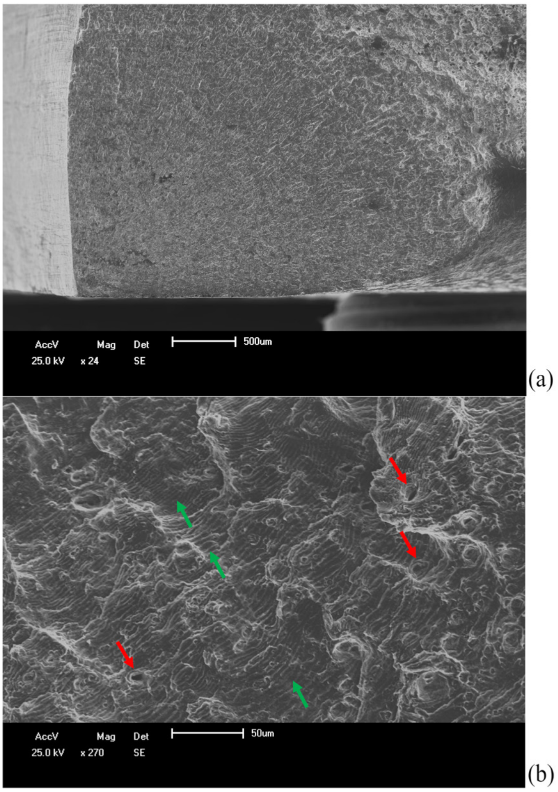

Figure 15. Fracture SEM image of (a) crack initiation region (5% pre-strain) and (b) region of stable crack propagation end (15% pre-strain).

In Figure 15b (green arrow), the presence of striations indicating fatigue failure can be observed[33]. However, these striations are not present in the stable crack propagation region but rather in the region preceding the final fracture zone. In this region, the loading is higher, and the material is already in the final phase of fatigue life. Associated with the striations, it is also possible to observe dimples (red arrow in Figure 15b), which are linked to the microvoid coalescence that occurs in the final fracture of the fatigue-tested specimen. This phenomenon is attributed to the remaining section exhibiting high ductility[33,34].

4. Conclusions

- As expected, the increase in tensile load led to an increase in the percentage of martensite in the AISI 304 austenitic steel specimens.
- There is a significant increase in residual stress values between samples with 0% deformation and 5% deformation.
- There are no significant changes in residual stress values with the increase in the percentage of martensite.
- The samples with higher fatigue resistance were those with 25% deformation or a higher percentage of martensite.
- The increase in magnetic permeability with percentual applied deformation is captured adequately by the MWM-Array method, which proves to be an interesting non-destructive technique for rapid scanning of components. The method generates an indicative map of martensitic transformation in different regions of AISI 304 steel-formed parts.

5. References

1. Hou Z, Xiu S, Yao Y, Sun C. The residual stress and martensitic transformation of 304 stainless steel in pre-stress grinding: influence and control on chloride induced SCC. J Mater Res Technol. 2023;24:4601-17.
2. Farias F, Alvarez-Armas I, Armas AF. On the strain-induced martensitic transformation process of the commercial AISI 304 stainless steel during cyclic loading. Int J Fatigue. 2020;140:105809.
3. Taleb L, Kpodekon C. Effect of pre-deformation on the cyclic behavior and fatigue of 304L SS. Key Eng Mater. 2016;703:125-31.
4. Li Y, San Martín D, Wang J, Wang C, Xu W. A review of the thermal stability of metastable austenite in steels: martensite formation. J Mater Sci Technol. 2021;91:200-14.
5. Hidalgo J, Findley KO, Santofimia MJ. Thermal and mechanical stability of retained austenite surrounded by martensite with different degrees of tempering. Mater Sci Eng A. 2017;690:337-47.
6. Zackay VF, Parker ER, Fahr D, Busch R. The enhancement of ductility in high-strength steels. Trans Am Soc Met. 1967;60(2):252-9.
7. Leffler B. Stainless steels and their properties. 2nd ed. Stockholm: Avesta Polarit; 1996.
8. Alves JM, Paula ADS, Brandao LP. Residual stress analysis after the induced martensitic transformation by rolling and tensile test in the 304L TRIP steel. Mater Res. 2021;24(4):e20210156. https://doi.org/10.1590/1980-5373-MR-2021-0156.
9. Ben Moussa N, Gharbi K, Chaieb I, Ben Fredj N. Improvement of AISI 304 austenitic stainless steel low-cycle fatigue life by initial and intermittent deep rolling. Int J Adv Manuf Technol. 2019;101:435-49.
10. Khan Z, Ahmed M. Stress-induced martensitic transformation in metastable austenitic stainless steels: effect on fatigue crack growth rate. J Mater Eng Perform. 1996;5:201-8.
11. Glage A, Weidner A, Biermann H. Effect of austenite stability on the low cycle fatigue behavior and microstructure of high alloyed metastable austenitic cast TRIPsteels. Procedia Eng. 2010;2(1):2085-94.
12. ASTM International. ASTM E8/E8M-21: Standard Test Methods for Tension Testing of Metallic Materials. West Conshohocken: ASTM International; 2021.
13. Dickson MJ. The significance of texture parameters in phase analysis by X-ray diffraction. J Appl Cryst. 1969;2(4):176-80.

14. ASTM International. ASTM E975-13: Standard Practice for X-Ray Determination of Retained Austenite in Steel with Near Random Crystallographic Orientation. West Conshohocken: ASTM International; 2013.
15. Faninger G, Hartmann U. Physikalische Grundlagen der quantitativen röntgenographischen Phasenanalyse (RPA). HTM. 1972;27(11):233-44.
16. Fitzpatrick ME, Lodini A, editors. Analysis of residual stress by diffraction using neutron and synchrotron radiation. London: CRC Press; 2003.
17. Hauk V. Structural and residual stress analysis by nondestructive methods: evaluation-application-assessment. Amsterdam: Elsevier; 1997.
18. Cullity BD, Stock SR. Elements of X-ray diffraction. 3rd ed. Harlow: Pearson Education Limited; 2014.
19. Msolli S, Martiny M, Costa Cardoso M, Pessanha Moreira L, Mercier S, Molinari A. Numerical modeling of the deformation of AISI 304L using a tangent additive Mori-Tanaka homogenization scheme: application to sheet metal forming. J Mater Process Technol. 2016;235:187-205.
20. ASTM International. ASTM E466-21: Standard Practice for Conducting Force Controlled Constant Amplitude Axial Fatigue Tests of Metallic Materials. West Conshohocken: ASTM International; 2021.
21. Fahr D. Stress- and strain-induced formation of martensite and its effects on strength and ductility of metastable austenitic stainless steel. Metall Trans. 1971;2:1883-92.
22. Zeng L, Song X, Chen N, Rong Y, Zuo X, Min N. A new understanding of transformation induced plasticity (TRIP) effect in austenitic steels. Mater Sci Eng A. 2022;857:143742.
23. Hedayati A, Najafizadeh A, Kermanpur A, Forouzan F. The effect of cold rolling regime on microstructure and mechanical properties of AISI 304L stainless steel. J Mater Process Technol. 2010;210(8):1017-22.
24. Martin S, Ullrich C, Šimek D, Martin U, Rafaja D. Stacking fault model of ∊-martensite and its DIFFaX implementation. J Appl Cryst. 2011;44(4):779-87.
25. Nakajima M, Akita M, Uematsu Y, Tokaji K. Effect of strain-induced martensitic transformation on fatigue behavior of type 304 stainless steel. Procedia Eng. 2010;2(1):323-30.
26. Alves JM, Brandao LP, Paula AS. Determination of phases and residual stresses after martensitic transformation induced by rolling in 304L stainless steel. Materia (Rio J). 2019;24(3):e12467. http://doi.org/10.1590/S1517-707620190003.0783.
27. ASTM International. ASTM E2860-20: Standard Test Method for Residual Stress Measurement by X-Ray Diffraction for Bearing Steels. West Conshohocken: ASTM International; 2021.
28. Cao B, Iwamoto T, Bhattacharjee PP. An experimental study on strain-induced martensitic transformation behavior in SUS304 austenitic stainless steel during higher strain rate deformation by continuous evaluation of relative magnetic permeability. Mater Sci Eng A. 2020;774:138927.
29. Washabaugh A, Grundy D, Goldfine N. Composite NDE using quasistatic electromagnetic. In: Proceedings of the SAMPE 2010 Conference; 2010 May 17-20; Seattle, WA: SAMPE Publishing. ; 2010. p. 1-14.
30. Cao B, Iwamoto T. An experimental study on strain rate sensitivity of strain-induced martensitic transformation in SUS304 by real-time measurement of relative magnetic permeability. Steel Res Int. 2017;88(12):1700022.
31. Al-Bakri AA, Sajuri Z, Abdulrazzaq M, Ariffin AK, Fafmin MS. Fatigue properties of strained thin 304 stainless steel sheets. Int J Automot Mech Eng. 2017;14(2):4171-82.
32. Parrington RJ. Fatigue fracture appearances. In: Miller BA, Shipley RJ, Parrington RJ, Dennies DP, editors. ASM handbook failure analysis and prevention. Vol. 11. Materials Park: ASM International; 2021. p. 343-55. http://dx.doi.org/10.31399/asm.hb.v11.a0006776.
33. Stevenson ME, Umberger PD, Uchneat SF. Fracture appearance and mechanisms of deformation and fracture. In: Seifi M, Bourell DL, Frazier W, Kuhn H, editors. Handbook of additive manufacturing design fundamentals and applications. Vol. 24A. Materials Park: ASM International; 2021. p. 273-303.
34. Sarkar A, Nagesha A, Parameswaran P, Sandhya R, Laha K, Okazaki M. Evolution of damage under combined low and high cycle fatigue loading in a type 316LN stainless steel at different temperatures. Int J Fatigue. 2017;103:28-38.